



## Abstract

Quantifying energy dissipation due to wave breaking remains an essential but elusive goal for studying and modeling air-sea fluxes of heat, gas, and momentum. Previous observations have shown that lifetimes of bubble plumes and surface foam are directly related to the dissipated energy. Specifically, the foam decay time can be used to estimate the timescale of the subsurface bubble plume and the energy dissipated in the breaking process. A mitigating factor is that the foam decay time can be significantly affected by the surfactant concentration. Here we present an experimental investigation of a new technique that exploits the thermal signature of cooling foam to infer wave breaking dynamics. The experiments were conducted in a laboratory wave tank using artificial seawater with and without the addition of a surfactant. We show that the time from the start of the breaking process to the onset of cooling scales with the bubble plume decay time and the dissipated energy, and is not significantly affected by the presence of additional surfactants. We confirm observations from the field of the spatial variability of the temperature of foam generated by an individual breaking event, which has implications for inferring the spatial variability of bubble plume depth.

## Plain Language Summary

Breaking waves cause mixing and are important for redistributing heat, transporting gases between the air and the water, and generating currents. Bubbles from breaking waves eventually rise and stay at the surface where they can be visually seen as foam. Scientists have found that the time it takes for the foam to disappear is related to the strength of the breaking waves. However, natural chemicals in the seawater can cause the bubbles to disappear more slowly, increasing the time they are seen at the surface. We present a new method to estimate when the bubble plume has decayed based on the foam temperature. We generate breaking waves in a laboratory and use an infrared camera to measure the temperature of the foam and find that the foam cools when bubbles stop rising. We varied the strength of the breaking waves and measured the cooling time for the foam to show that larger, stronger breaking waves cause a longer time before the foam begins to cool. When we added chemicals to increase the time foam stays at the surface, the cooling time remains about the same, even though the foam is still seen at the surface for a longer time.

## 1 Introduction

Wave breaking plays a critical role in air-sea interaction processes in both the open ocean and the surf zone. The energy transferred from the atmosphere to the ocean through wind-wave generation is ultimately dissipated by wave breaking. Therefore, quantifying the energy dissipation due to wave breaking is directly relevant to wave prediction models used for operational sea-state forecasting and the impact of waves on coastal regions. At high wind speeds, bubbles generated by large scale breaking waves are the primary mechanism for gas transfer and dominate the energy dissipation due to breaking (Lamarre & Melville, 1991). Bubbles generated by breaking waves also contribute to marine aerosol formation through spray droplets produced when foam bubbles burst at the surface (Veron, 2015; Erinin et al., 2019, and references therein). Foam generated by wave breaking has increased reflectivity of solar radiation that can affect the earth's albedo (Evans et al., 2010; Gordon & Jacobs, 1977) and the enhanced microwave emissivity of foam impacts space-borne radiometer measurements of wind speed. In short, wave breaking is an important mechanism for fluxes of momentum, gas, and heat across the air-water interface and for global ocean remote sensing applications. Here we focus on breaking waves that produce visible foam.

A wave begins to break when the forward face steepens and the crest becomes unstable. The morphology of an individual breaking wave that generates foam is generally categorized as either spilling or plunging. Plunging breakers occur when a wave crest forms an open curl and rapidly falls forward. Spilling breakers are characterized by a wave crest that spills

61 forward and rolls down the face. For both types, subsurface bubble plumes are generated  
 62 by the impact of the overturning crest on the water surface. For plunging breakers, bubbles  
 63 are also injected when the air pocket formed by the curling crest collapses, and by the jet  
 64 impinging on the surface (Kiger & Duncan, 2012). As the actively breaking crest continues  
 65 to propagate for the breaker lifetime, a bubbly turbulent wake is left behind. Bubbles rise to  
 66 the surface and produce patches of residual surface foam as turbulence in the wake subsides.

67 The term whitecap has been used to describe both the foam generated by the actively  
 68 breaking crest and the residual foam left behind in the wake. Monahan and Lu (1990)  
 69 denoted the actively breaking period as stage-A and the period following as stage-B. Stage-  
 70 A also has been referred to as the “acoustically active” period (Deane & Stokes, 2002),  
 71 because the formation and fragmentation of bubbles generate underwater sound during this  
 72 period. Stage-A includes the formation of the actively breaking crest and creation of the  
 73 bubble plume and ends when air is no longer actively entrained. Stage-B includes the  
 74 expansion and rise of the bubble plume as well as the formation and decay of the resulting  
 75 residual foam and typically is of longer duration than stage-A (Kleiss & Melville, 2010;  
 76 Monahan & Lu, 1990).

77 Whitecap coverage,  $W$ , is the percentage area of the sea surface covered by foam mea-  
 78 sured from visible imagery. Techniques for measuring  $W$  have evolved from labor-intensive  
 79 analysis of individual photographs (Monahan, 1969) to automated techniques using high-  
 80 resolution digital imagery (Callaghan & White, 2009). Scanlon and Ward (2013) recently  
 81 reported on a manual technique to separate active and maturing whitecaps, but automated  
 82 processing of visible imagery remains a challenge. Most visible measurements of  $W$  include  
 83 both stages of whitecap foam because of the difficulty of objectively and automatically dis-  
 84 tinguishing between stage-A and stage-B foam. However, there is strong motivation to be  
 85 able to separately measure whitecap coverage for stage-A,  $W_A$ , and for stage-B,  $W_B$ , in  
 86 order to examine the different processes of interest that are associated with the different  
 87 stages. For instance,  $W_A$  is the appropriate coverage to determine the breaking rate and for  
 88 correlation with the energy dissipation (Kleiss & Melville, 2010) while  $W_B$  has been related  
 89 to sea-salt aerosol production due to the preponderance of bursting bubbles as the foam  
 90 dissipates (Callaghan, 2013; Monahan et al., 1986).

91 Since wave breaking is driven by wind stress, many authors have pursued a fundamental  
 92 parameterization of  $W$  with wind speed. A compilation of historical data sets by Anguelova  
 93 and Webster (2006) shows scatter of  $W$  versus wind speed of over three orders of magnitude,  
 94 suggesting other factors need to be considered. Recent results by Callaghan et al. (2008,  
 95 2012, 2013) indicate that potential contributors to the observed scatter of  $W$  with wind  
 96 speed include environmental parameters such as wave field characteristics, breaker type,  
 97 and surfactant effects as well as differences in image acquisition and analysis techniques.  
 98 Variations in the decay time of oceanic whitecap foam led Callaghan et al. (2012) to speculate  
 99 that the two primary mechanisms that cause scatter of whitecap coverage with wind speed  
 100 are (i) the effect of surfactants on foam stability and (ii) differences between bubble plume  
 101 characteristics caused by variation in breaker type.

102 In the laboratory, Callaghan et al. (2013) investigated these two mechanisms by compar-  
 103 ing the visible decay times for foam,  $\tau_{\text{foam}}$ , and for the bubble plume,  $\tau_{\text{plume}}$ , for whitecaps  
 104 generated by focused wave packets using clean and surfactant-contaminated (Triton X-100  
 105 at  $204 \mu\text{gr}\cdot\text{L}^{-1}$ ) seawater. They found that  $\tau_{\text{plume}}$  was proportional to the increase in energy  
 106 dissipated as the scale of breaking ranged from spilling to plunging. However, when surfac-  
 107 tants were present, the scaling between  $\tau_{\text{foam}}$  and  $\tau_{\text{plume}}$  varied significantly. Surfactants  
 108 act to stabilize the bubbles, causing them to persist at the surface after the bubble plume  
 109 has decayed and the foam generation process has ceased. For clean conditions, the foam  
 110 decay time can provide a direct estimate of the plume degassing time. In the presence of  
 111 surfactants, their effect on increasing the foam decay time needs to be accounted for in order  
 112 to infer the plume decay time (Callaghan et al., 2017).

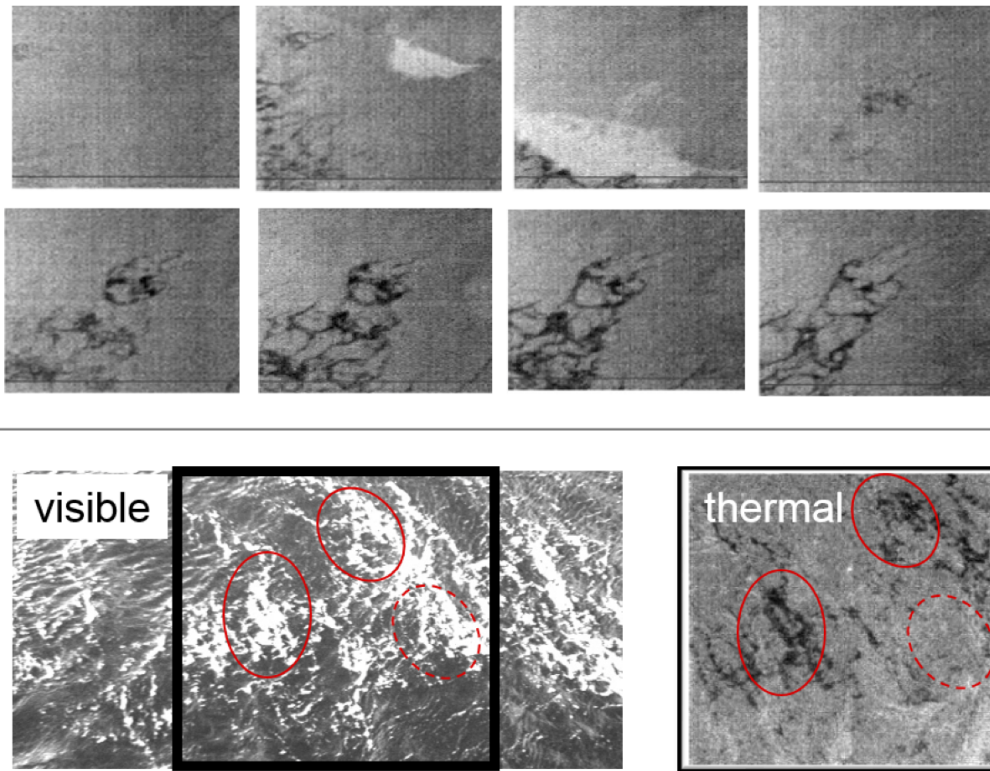


**Figure 1.** (Top) An examples of infrared image sequences showing the cooling of residual foam in the wake of a breaking wave in the open ocean. Time increases left to right then top to bottom. Lighter shades of gray are warm and darker shades are cold. Image size is approximately  $5 \text{ m} \times 5 \text{ m}$ . (Bottom) Simultaneous visible (left) and infrared (right) images of residual foam in the wake of a breaking wave in the open ocean. Solid ovals indicate locations where visible foam appears cool while foam does not appear cool in the dashed oval (Fogelberg, 2003).

113 The infrared image sequence in Figure 1 illustrates the rapid cooling of foam left behind  
 114 after the passage of a breaking wave, similar to observations reported by Fogelberg (2003)  
 115 and Marmorino and Smith (2005). Recent laboratory findings by Chickadel et al. (2014) that  
 116 the heat flux from foam is three to four times greater than foam-free water are consistent  
 117 with the suggestion by Marmorino and Smith (2005) that the cooling is due to enhanced  
 118 evaporation from bubbles. Chickadel et al. (2014) also reported that the foam cooling begins  
 119 after the foam-producing bubbles cease rising. The foam cooling phenomenon has been used  
 120 recently to distinguish between the active and residual foam. In the open ocean, Potter et  
 121 al. (2015) used infrared imagery to quantify the lifetime stages and characterize properties of  
 122 the active and residual whitecaps. In the surf zone, Carini et al. (2015) used the difference in  
 123 the thermal signature of active and residual foam to identify and extract the perpendicular  
 124 crest length of the aerated breaking region.

125 A consistent observation in the field is that there is a momentary delay of  $O(1 \text{ s})$  between  
 126 when the foam appears in the visible and when it appears cool in the infrared. The foam  
 127 is generated by air entrainment and bubbles at the surface so its initial temperature will be  
 128 approximately the same as that of the surface water. As the breaking process continues,  
 129 the surface foam is replenished from below by bubbles rising to the surface from the plume.

130 Since the heat flux for foam is three to four times greater than that for foam-free water, the  
 131 delay in the appearance of cool foam implies that the surface of the foam is replenished by  
 132 near-surface water from below at a rate such that there is not enough time for it to cool.  
 133 That is, the rate of replenishment of the foam overcomes the cooling rate. As the bubble  
 134 plume decays and the foam replenishment rate lessens, the foam will begin to cool and its  
 135 temperature will drop. Thus the time between the onset of breaking and the appearance  
 136 of cool foam should be related to the timescale of the bubble plume decay. Additionally,  
 137 field observations show that not all residual foam from a given breaking event begins to cool  
 138 at the same time. The simultaneous visible and infrared images in Figure 1(bottom) show  
 139 two regions outlined by solid ovals where foam is cooler than the undisturbed surface while  
 140 in the dashed oval region the foam temperature is comparable to the undisturbed surface.  
 141 Since the foam in Figure 1(bottom) was generated at the same time, the delay in the onset  
 142 of cooling at different locations implies that the bubble plume depth was greater for the  
 143 location with longer onset times.

144 Here we seek to exploit the thermal signature of the cooling of surface foam in the  
 145 wake of a breaking wave to infer subsurface plume dynamics. Our long-term goal is to  
 146 develop a new remote sensing technique that will simultaneously provide (1) a measurement  
 147 of the bubble plume timescale relevant to estimating dissipation and (2) a map of the spatial  
 148 variability of the bubble plume depth. Thus our objectives are to test the following two  
 149 hypotheses:

- 150 1. The time from the start of breaking to the onset of foam cooling scales with the  
 151 bubble plume decay time.
- 152 2. For an individual breaking event, the spatial variability of the bubble plume depth  
 153 can be inferred by the spatial variability of the time for the onset of foam cooling.

154 With regard to Hypothesis (1), we seek to show that while the foam at the surface  
 155 is being replenished from below, its temperature remains comparable to that of the water  
 156 from which it is generated. The cooling begins only when the rate of replenishment by the  
 157 rising bubbles is less than the foam cooling rate. The start of the cooling is delayed for more  
 158 energetic breaking waves that generate larger and deeper bubble plumes compared to less  
 159 energetic breakers that generate smaller and shallower plumes. With regard to Hypothesis  
 160 (2), we seek to confirm in the laboratory the observations from the field of the spatial  
 161 variability of the temperature of foam generated at the same time by an individual breaking  
 162 event. A complete test of Hypothesis (2) requires subsurface measurement of the spatial  
 163 variability of bubble plume depth and size distribution, which is beyond the scope of this  
 164 effort. However, the spatial variability of the surface foam temperature can be observed in  
 165 infrared imagery.

166 We present a new approach for estimating the timescale of the subsurface bubble plume  
 167 based on the timescale of the cooling foam. The results from our laboratory experiments  
 168 show that the onset of cooling of the foam scales with a measure of the decay time of the  
 169 bubble plume and that the cooling onset time varies spatially for foam simultaneously  
 170 generated by an individual event. The cooling time is not significantly affected by sur-  
 171 factants, which is in contrast to the finding that foam persist longer when surfactants are  
 172 present (Callaghan et al., 2013). We demonstrate that infrared imagery can provide the  
 173 ability to infer the bubble plume decay time and thus provide a measure of wave energy  
 174 dissipation. We also confirm in the laboratory the observations from the field of the spatial  
 175 variability of the temperature of foam generated at the same time by an individual breaking  
 176 event.

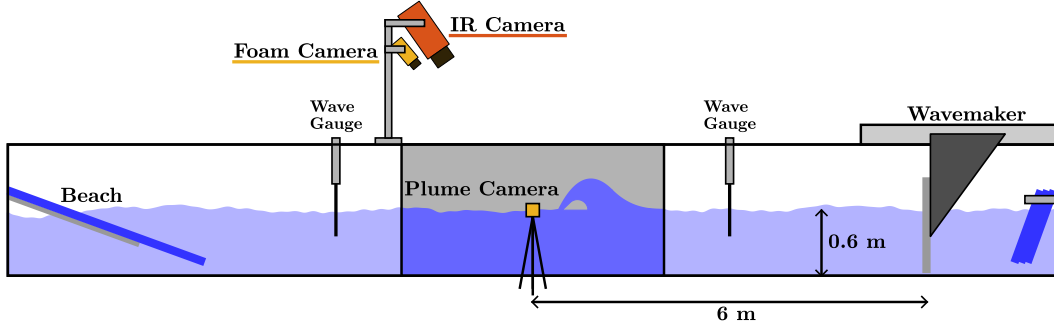


**Figure 2.** Schematic of the experimental setup. One side wall of the tank is made of glass for optical access. The other side wall is painted black in a 1.6 m long test section. The top of the tank is covered except for the test section. The waves are designed to break at a location approximately 6 m from the wave paddle. The tank width is 0.91 m.

## 2 Experimental Details

### 2.1 Setup

The experiments were performed in the Washington Air-Sea Interaction Research Facility (WASIRF) wave flume at the University of Washington (Figure 2). The wave flume is 12 m long, 0.91 m wide, and 1.2 m tall, with one side wall made of glass that allows optical access. The top of the tank was covered with removable panels except for the test section that was left open for imaging. The facility includes a water circulation system that is equipped with an inline filter and electric heater. The flume was filled with salt water to a depth of 0.6 m using Instant Ocean and tap water. The salinity was set to 30 ppt and was frequently checked with a refractometer to ensure it remained constant during the experiments.

A programmable piston-type wavemaker at one end of the tank was used to generate breaking waves. The wavemaker consists of a flat rectangular paddle that is 0.9 m tall and spans the tank width and extends to the bottom of the tank. The motion of the wavemaker is controlled by an analog signal sent to the controller of the servo motor. Wave absorbing beaches were installed at both ends of the tank to diminish wave reflection from the end walls.

### 2.2 Wave Generation

Breaking waves are generated using the dispersive focusing wave packet technique used extensively in laboratory experiments (Rapp & Melville, 1990; Duncan et al., 1999; Drazen et al., 2008; Wang et al., 2018). In this technique, a packet is composed of many components and is designed such that all the components have the same phase at a prescribed “breaking” location. In the experiments presented here, the motion of the wavemaker can be described as

$$\eta_0 = \sum_{i=1}^N \frac{a_i}{a_i^{corr}} \cos(-k_i x_b - 2\pi f_i(t - t_b) - \phi_i^{corr}) \quad (1)$$

where  $\eta_0$  is the wavemaker horizontal displacement,  $N = 32$  is the total number of components, and for each component,  $a_i$  is the amplitude,  $a_i^{corr}$  is the amplitude correction factor found in the calibration process,  $k_i$  is the wavenumber,  $f_i$  is the frequency, and  $\phi_i^{corr}$  is the phase correction.  $x_b$  and  $t_b$  are the theoretical breaking location and time, respectively. Equation (1) produces a periodic signal and needs to be windowed to provide the proper wavemaker motion. We used a window with hyperbolic tangent edges to taper the signal

207 in a smooth fashion. The parameters that control the shape of the wave packet signal and  
 208 the breaking location of the waves are the central frequency of the packet,  $f_c = 0.88$  Hz,  
 209 the frequency bandwidth,  $\Delta f = 0.5f_c$ , and the normalized breaking location,  $x_b k_c = 33$ ,  
 210 where  $k_c$  is the wavenumber corresponding to the central frequency. These parameters were  
 211 chosen to generate breaking waves with similar shape but with considerable difference in  
 212 foam generation, plume depth, and energy dissipation. The global slope of a wave packet is  
 213 used as the control parameter for the scale of the breaking waves and is defined as:

$$S = \sum_{i=1}^N a_i k_i \quad (2)$$

214 Following Loewen (1991), all the components in the wave packet are chosen to have the  
 215 same slope. Hence, increasing the global slope,  $S$ , is essentially equivalent to multiplying  
 216 the signal by a constant factor without changing the overall shape.

### 217 **2.3 Measurement Techniques**

218 The bubble plume and the surface foam generated by breaking waves were measured  
 219 using two identical visible cameras (Point Grey model Blackfly; 4 MP, 15 fps) to visualize  
 220 the light scattered by the bubbles against the dark background in the test section, which was  
 221 illuminated by two LED light sources. The bubble plume camera was located outside the  
 222 glass side wall of the tank and was oriented normal to the wall. The horizontal center-line  
 223 of the field of view coincided with the calm water surface. The field of view of this camera  
 224 was approximately  $1.2 \text{ m} \times 1.2 \text{ m}$ . The foam camera was located approximately 2 m above  
 225 the water surface and viewed the surface at an incidence angle of 30 degrees. The field of  
 226 view of this camera extended to regions outside of the tank and these regions were masked  
 227 in the analysis.

228 The surface temperature was measured using an uncooled, longwave (7-14  $\mu\text{m}$ ) infrared  
 229 camera (DRS model UC640;  $640 \times 480$  pixels, 30 fps, NEDT 25 mK) that was mounted ad-  
 230 jacent to the foam camera. The foam and infrared cameras had overlapping fields of view  
 231 and a transformation map between the two cameras was found in the calibration process. A  
 232 circular metal target was attached to a float on the water surface and heated before being  
 233 placed inside the tank so it would be visible to the infrared camera. The target was then  
 234 moved in different parts of the field of view and imaged by the two cameras simultaneously.  
 235 The center of the circular target was tracked through the image sequences and the transfor-  
 236 mation between the two cameras was found using a projective transformation between the  
 237 pairs of target locations (Goshtasby, 1986). A second transformation was found and applied  
 238 to all infrared and visible images to account for the oblique perspective of these cameras.

239 The two visible cameras and the infrared camera were time-synchronized through the  
 240 data collection software to record the breaking process simultaneously. Two capacitance-  
 241 type wire wave gauges were mounted approximately 1.5 m upstream and downstream of  
 242 the breaking location. The surface elevation data recorded at these locations were used to  
 243 estimate the total energy dissipated by the breakers (Rapp & Melville, 1990).

### 244 **2.4 Experimental Procedures and Conditions**

245 For the experiments presented here, four breakers with slope values of  $S = 0.34, 0.35,$   
 246  $0.36,$  and  $0.37$  were used. This range of slopes corresponds to plunging breakers that vary in  
 247 intensity, amount of air entrained, and energy dissipation. This range of slopes corresponds  
 248 to a range of  $E = 74\text{-}105 \text{ J/m}$  (along the crest of wave) in energy dissipation. Properties of  
 249 the breakers are listed in Table 1.

250 The data collection process was automated so that many runs could be carried out  
 251 unattended. The water in the tank was recirculated and filtered the night before each ex-  
 252 periment day for about eight hours. In the morning of each experiment day, the water was

**Table 1.** Properties of the breaking waves used in the experiments where  $d_{\max}$  is the maximum depth of the bubble plume,  $\Delta E$  is the total energy dissipation as estimated by upstream and downstream wave gauges,  $A_{\text{plume}}^{\max}$  is the maximum plume area, and  $A_{\text{foam}}^{\max}$  is the maximum whitecap area.

| Slope                                       | 0.34               | 0.35               | 0.36               | 0.37               |
|---|--------------------|--------------------|--------------------|--------------------|
| $\Delta E$ (J/m)                            | 73.93              | 85.23              | 93.69              | 105.03             |
| $d_{\max}$ (cm)                             | $15.05 \pm 1.64$   | $18.48 \pm 1.71$   | $24.79 \pm 2.98$   | $29.12 \pm 3.21$   |
| $A_{\text{plume}}^{\max}$ (m <sup>2</sup> ) | $0.085 \pm 0.0066$ | $0.113 \pm 0.0079$ | $0.141 \pm 0.0081$ | $0.158 \pm 0.0105$ |
| $A_{\text{foam}}^{\max}$ (m <sup>2</sup> )  | $0.599 \pm 0.038$  | $0.728 \pm 0.045$  | $0.808 \pm 0.065$  | $0.864 \pm 0.058$  |

253 heated to approximately 1 degree Celsius above the ambient air temperature. The air tem-  
 254 perature varied slightly during the experiments due to the diurnal cycle. The temperature  
 255 difference,  $\Delta T = T_{\text{water}} - T_{\text{air}}$ , was in the range of zero to 2 °C for all the experimental runs  
 256 presented here. The wavemaker and the data collection computers were set up to contin-  
 257 uously generate breaking waves and collect data every ten minutes over the course of the  
 258 day. This time between runs was found to be sufficient for the wave reflections to dissipate.

259 Two sets of experiments were carried out; in the first set, clean salt water was used  
 260 (no additional surfactants), and in the second set, Triton X-100 was added to achieve a  
 261 concentration of 200  $\mu\text{g/L}$ . For each wave slope and for a condition with or without additional  
 262 surfactants (eight total cases), between 50 to 60 runs were recorded and analyzed for a total  
 263 of 462 individual breaking waves overall.

### 264 3 Image Processing

265 A sequence of visible bubble plume and foam images for a breaker propagating from  
 266 left to right are shown in Figure 3 (see the supplementary material for movies corresponding  
 267 to the image sequences). The images are separated by  $\Delta t = 1/3$  s and the first image in  
 268 the sequence is from  $t = 1/3$  s. The time origin,  $t = 0$ , denotes the start of the breaking  
 269 process and is found by manually inspecting the bubble plume camera images. For the  
 270 example shown in Figure 3 (top), which is the largest wave slope used, a significant amount  
 271 of air is entrained and left behind by the active breaker in (a) and (b). Two relatively  
 272 large and distinct bubble plumes occur for this breaker, as seen in images (c) and (d). The  
 273 bubbles quickly rise to the surface in (e) and (f), and the residual surface foam left behind  
 274 is apparent in (g) and (h).

275 The gray-scale visible images shown in Figure 3 were analyzed to obtain foam and  
 276 plume area time series. First, the background was subtracted from all images in a sequence  
 277 to enhance the signal and reduce the effect of non-uniformity in the lighting condition.  
 278 Then, a manually determined intensity threshold was applied to segregate the bright foam  
 279 and bubbles from the dark background, resulting in black and white (B/W) image masks.  
 280 The threshold was chosen to include all visible foam and bubbles, regardless of size or  
 281 brightness. The same fixed threshold was used for all the runs since the lighting conditions  
 282 were invariant. For the foam images, bright regions smaller than 200 pixels were removed  
 283 from the images to reduce the speckle noise. Dark areas smaller than 200 pixels that are  
 284 enclosed by bright foam were converted to white pixels. These regions are typically centers  
 285 of large bubbles before they burst at the surface. The foam images were then transformed  
 286 into the coordinate system of the infrared camera. A sequence of the resulting B/W bubble  
 287 plume and foam masks is shown in Figure 4. This processing was done in the range of  
 288  $t = -1$  s to  $t = 10$  s for each run (166 frames per run).

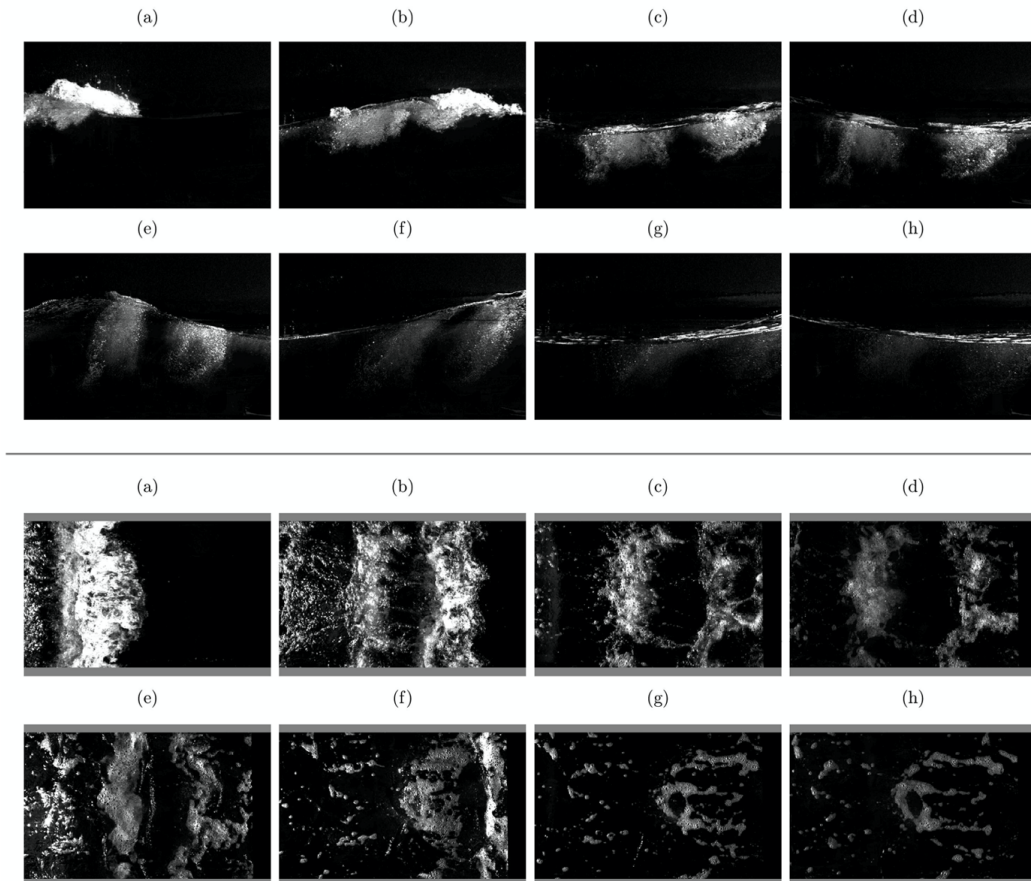


**Figure 3.** A sequence of visible images of a breaking wave with a slope of  $S = 0.37$ . The wave is propagating from left to right. The frames are separated in time by  $1/3$  s. The wave packets are designed so that the breaking occurs at the edge of the field of view. (Top) bubble plume images taken from the camera that is looking through the glass wall of the tank. (Bottom) visible foam images taken by the camera that is looking down at the water surface. The foam images are shown in the coordinate system of the infrared camera images (see text). Each image is approximately 1.2 m long. This figure corresponds to Movie S2 in the supplementary information.

289 The sequence of infrared images of the surface in Figures 5 are from the individual run  
 290 corresponding to the visible imagery in Figures 3 and 4. The blue lines are the boundaries  
 291 of the regions covered by the visible foam and are derived from the masks in Figure 4. The  
 292 images show the temperature anomaly, defined as the difference between the instantaneous  
 293 temperature and the background reference temperature. The background reference temper-  
 294 ature for each individual run was the maximum value of the spatially-averaged temperature  
 295 of the field in the time span of  $0 < t < 10$  s. The temperature range is shown in the colorbar  
 296 with dark corresponding to cold and bright to warm.

297 At the beginning of the breaking process, the cool skin layer is destroyed so that the skin  
 298 temperature during breaking and in the wake is approximately equal to the bulk temperature  
 299 (Jessup et al., 1997). As the crest begins breaking in Figure 5(a), the nearly uniform  
 300 disruption of the cool skin layer produces a front of warm foam over the entire width of  
 301 the tank that advances with the crest. In frames (a)-(c), the temperature of the surface  
 302 disrupted by the breaking crest is nearly uniform, regardless of whether it is foam-covered or

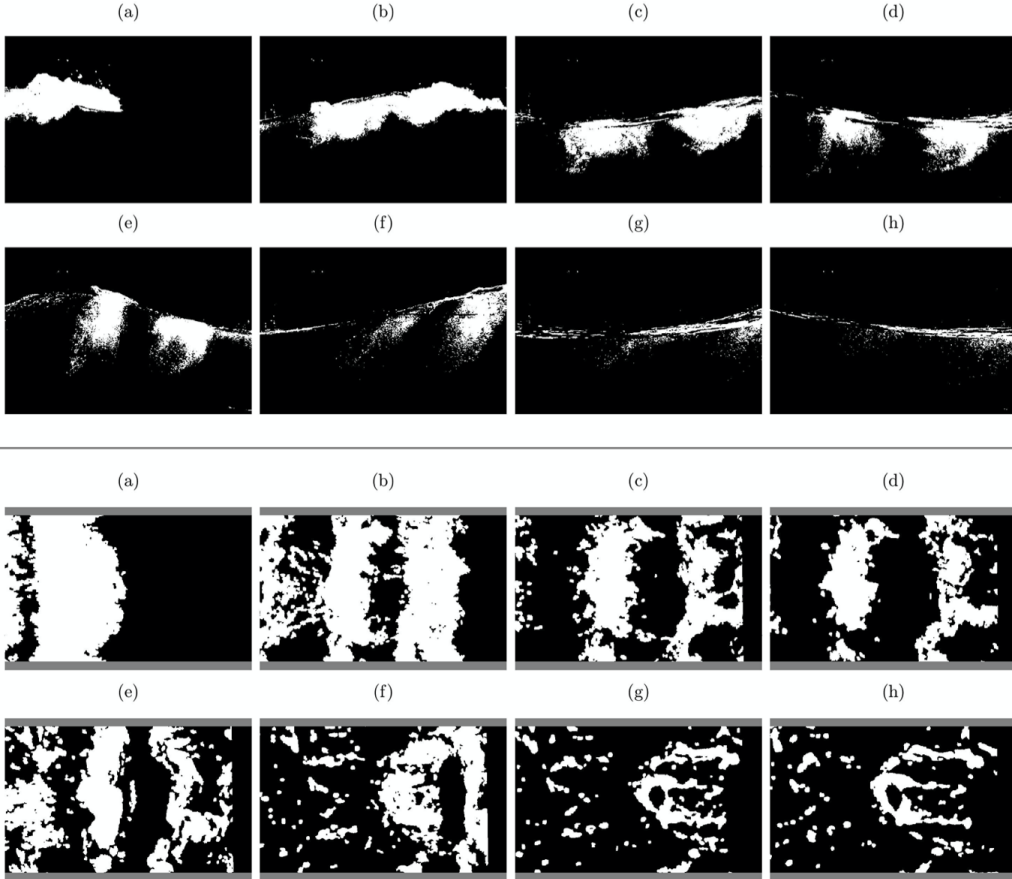


**Figure 4.** A sequence of thresholded B/W images of a breaking wave with a slope of  $S = 0.37$  corresponding to the images in Figure 3.

303 foam-free. The foam begins to cool in (d) but the degree of cooling is not spatially uniform  
 304 over the foam until the end of the sequence in (g)-(h). This spatial variation is apparent  
 305 between the two main foam regions in (d) and (e). Eventually, the foam dissipates and  
 306 after several minutes (not shown in the figure), the cool skin layer recovers and the surface  
 307 temperature drops to its value before the disruption by the breaking wave.

308 The image sequences of the surface foam and bubble plume in Figures 3 and 4 and  
 309 the foam temperature anomaly in Figure 5 are consistent with the conceptual relationship  
 310 presented in the discussion of Figure 1 (bottom). That is, while the surface foam is being  
 311 renewed by rising bubbles from below during the active breaking process, its temperature  
 312 is comparable to that of the surrounding foam-free water. As the bubble plume decays and  
 313 the renewal rate decreases, the enhanced heat flux of the foam causes its temperature to  
 314 drop. A schematic representation of the conceptual relationship between the foam or bubble  
 315 plume area and foam temperature anomaly is illustrated in Figure 6. The area exhibits a  
 316 growth phase, characterized by a rapid increase from when breaking begins at  $t = 0$  to a  
 317 maximum, followed by a decay phase of varying duration. The foam temperature anomaly  
 318 also increases rapidly from  $t = 0$  but remains elevated for some finite time until the renewal  
 319 of the foam from below is reduced to the point where it no longer inhibits the cooling. The  
 320 primary time variables used in our analysis shown in the figure are:  $t_{\text{cool}}$ , the time from  
 321  $t = 0$  to the onset of foam cooling;  $t_{\text{max}}$ , the time from  $t = 0$  to the maximum area; and

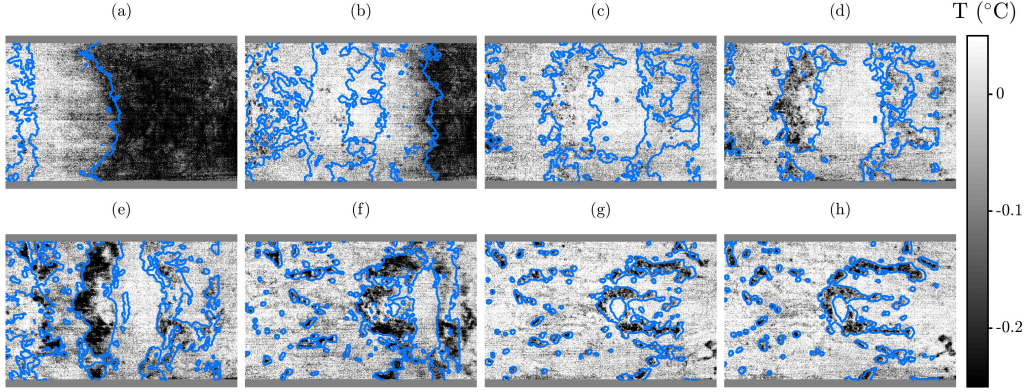


**Figure 5.** A sequence of infrared images of the surface temperature anomaly corresponding to the images in Figure 3. The temperature range is shown in the colorbar with dark meaning cold and bright meaning warm. The blue outlines show the location of the foam extracted from the visible foam images (Figure 4). This figure corresponds to Movie S2 in the supplementary information.

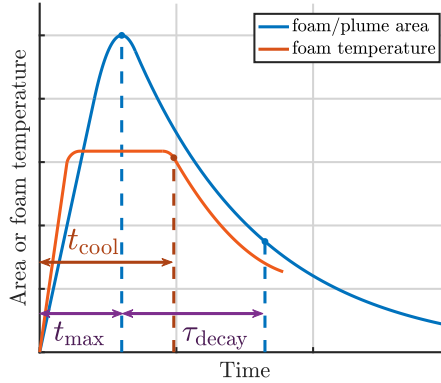


**Figure 6.** Schematic representation of conceptual relationship between the foam or bubble plume area (blue) and the foam temperature (orange) showing relevant time variables:  $t_{\text{cool}}$ , the time from  $t = 0$  to the onset of foam cooling;  $t_{\text{max}}$ , the time from  $t = 0$  to the maximum area; and  $\tau_{\text{decay}}$ , the area decay timescale equal to the e-folding time of the decay from the maximum area. The total bubble plume timescale (not shown) is defined as  $\tau_{\text{plume}}^{\text{total}} = t_{\text{plume}}^{\text{max}} + \tau_{\text{plume}}^{\text{decay}}$ .

322  $\tau_{\text{decay}}$ , the area decay timescale equal to the e-folding time of the decay from the maximum  
 323 area. The total bubble plume timescale (not shown) is defined as  $\tau_{\text{plume}}^{\text{total}} = t_{\text{plume}}^{\text{max}} + \tau_{\text{plume}}^{\text{decay}}$ .

#### 324 4 Results and Discussion

325 The B/W masks in Figure 4 were used to calculate the foam and bubble plume areas.  
 326 The foam coverage is defined as the fraction of the image area that is covered by the foam  
 327 in each B/W mask. The bubble plume area was similarly extracted from the B/W bubble  
 328 plume masks. In each plot of foam and bubble plume area time series shown in Figure 7,  
 329 the thick lines are the ensemble averages for each condition (slope and surfactant) and the  
 330 shaded areas show one standard deviation of the samples. Both the foam and bubble plume  
 331 areas exhibit a growth and decay phase as illustrated in Figure 6.

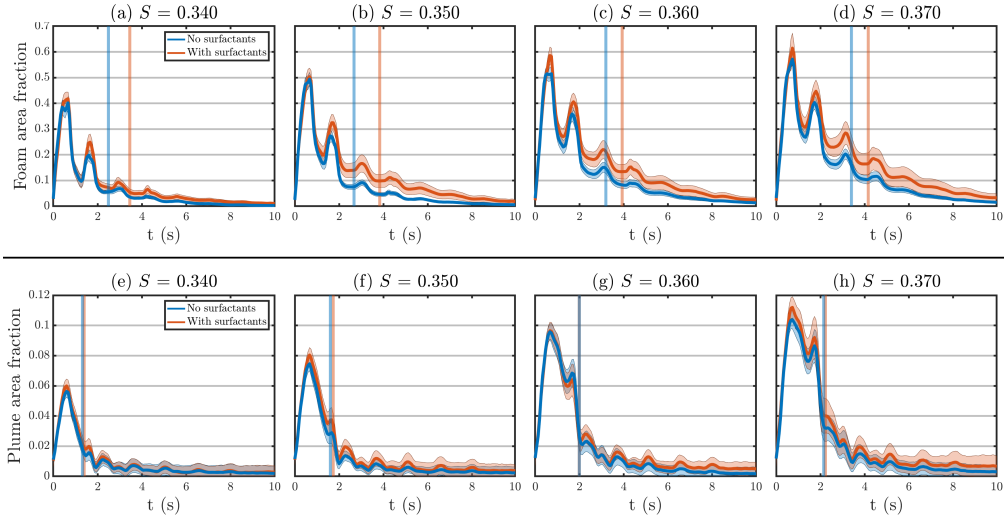


**Figure 7.** Time series of the foam area (top) and the bubble plume cross-sectional area (bottom). The area is normalized by the image size. The thick lines are the ensemble averages for each condition (slope and surfactant) and the shaded areas show one standard deviations of the samples. The vertical lines indicate the location of the e-folding time from the maximum relative to time  $t=0$ .

332 Figure 7(a-d) shows the time series of the foam coverage for each wave packet. The  
 333 oscillations in the foam and the bubble plume coverage during the decay phase and the  
 334 existence of local peaks in the time series are due to the orbital motion of the surface  
 335 waves which causes the surface foam and the bubble plume to expand and contract, and be  
 336 advected in and out of the field of view. The amount of foam generated by the breaking  
 337 waves increases with the slope of the wave packet. Initially, there is little difference between  
 338 clean water and surfactant-added cases. However, the longevity of the foam is increased for  
 339 the cases with additional surfactants, as is apparent from the foam coverage values at later  
 340 times. Furthermore, there is more variation in the amount of foam among individual runs  
 341 with the same experimental condition for the cases with additional surfactants, especially  
 342 at later times.

343 The time series of the bubble plume area are shown in Figure 7(e-h). Similar to the  
 344 foam coverage, the maximum bubble plume area increases with the wave packet slope but  
 345 there is little difference between the clean water and surfactant-added cases, both in the  
 346 amount and the persistence of the bubbles. The second peak in these plots (at  $t \approx 2$  s) is  
 347 primarily caused by the rapid upward motion of the free surface that results in the stretching  
 348 and dilation of the bubble plume (see Figure 4-e). The variations in the plume area values  
 349 among different runs for  $t > 4$  s is due to the residual surface foam appearing in the bubble-  
 350 plume camera. This contamination of the plume area was reduced through processing and  
 351 did not affect the correlation with the cooling time, presented below.

352 The visible foam decay timescale,  $\tau_{\text{foam}}^{\text{decay}}$ , and the bubble plume decay timescale,  $\tau_{\text{plume}}^{\text{decay}}$ ,  
 353 for each experimental run were calculated from their corresponding time series. An expo-  
 354 nential function in the form of  $A_* = A_*^{\text{max}} \exp(-t/\tau_*^{\text{decay}})$ , where  $*$  = (foam, plume), was fit  
 355 to the data between the time of maximum area and the time when the area drops below  
 356 a threshold. The average values of the maximum foam and bubble plume areas for each  
 357 slope are listed in Table 1. The fitted curve was constrained to include the maximum area  
 358 data point. The threshold used for the foam time series was 5% of the maximum area.  
 359 For the plume area time series, the threshold was varied for different wave packet slopes to

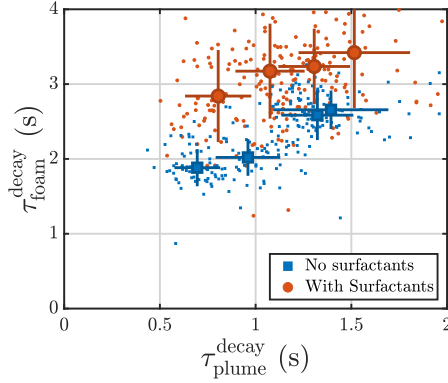


**Figure 8.** Visible foam timescale  $\tau_{\text{foam}}^{\text{decay}}$  versus bubble plume timescale  $\tau_{\text{plume}}^{\text{decay}}$ . Each small symbol represents one experimental run. The large symbols are the mean value for each wave packet slope  $S$ . The error bars show one standard deviations of the samples.

360 reduce the fitting error due to the influence of the residual foam at the surface, which could  
 361 be detected as bubble plume by the processing algorithm. The threshold values for these  
 362 cases were between 0.2 and 0.4 of the maximum plume area. The locations correspond-  
 363 ing to the decay of the foam and plume area curves to a value of  $1/e$  from their maxima  
 364 are indicated in Figure 7 by vertical lines for both the surfactant-free and surfactant-added  
 365 cases. Thus the magnitude of the timescales is given by the time between the maximum and  
 366 the corresponding vertical line (Figure 6). The difference between the surfactant-free and  
 367 surfactant-added cases is readily apparent for the visible foam timescale while practically  
 368 no difference occurs for the plume timescale.

369 Figure 8 shows that the visible foam timescale  $\tau_{\text{foam}}^{\text{decay}}$  increases approximately linearly  
 370 with the bubble plume decay timescale  $\tau_{\text{plume}}^{\text{decay}}$ , which is consistent with the results of  
 371 Callaghan et al. (2013). They found a 1:1 correspondence for surfactant-free conditions,  
 372 whereas the slope of the surfactant-free correlation for our measurements is approximately  
 373 2. While our bubble plume decay times for surfactant-free conditions are comparable to  
 374 theirs, our foam decay times are about twice as large. Since the foam lifetime is known  
 375 to be a function of salinity and seawater composition, the most likely reason for the dif-  
 376 ference in foam decay time and slope is that we used artificial seawater (Instant Ocean)  
 377 while Callaghan et al. (2013) used filtered natural seawater. We found that adding sur-  
 378 factants increased the foam area decay time by an average of 32%. Furthermore, the slope of  
 379 the approximately linear behavior with surfactants is comparable to that for surfactant-free  
 380 conditions. Although Callaghan et al. (2013) also found an increase in foam decay time  
 381 with surfactants, they reported a significantly larger slope than we found. In addition to  
 382 the effects of using different types of sea water, another possible difference that could affect  
 383 the magnitude of the surfactant effect and resulting slope is the unknown level of surfactants  
 384 that may have been present for the surfactant-free conditions.

385 The foam temperature anomaly was calculated for each run using the foam mask se-  
 386 quence extracted from the visible foam images (e.g. Figure 4). This mask was then applied  
 387 to the corresponding frames of the infrared sequence to isolate the regions covered by the  
 388 foam from the rest of the image. The time series of the mean foam temperature anomaly,  
 389  $T_{\text{foam}}$ , is plotted in Figure 9(a-d) for each experimental condition. Immediately after the  
 390 start of the breaking process, the foam temperature increases because of the disruption of  
 391 the cool skin layer. The foam temperature plateaus for a short but significant time and then  
 392 starts to cool. These plots show that the duration of the plateau in foam temperature in-  
 393 creases with the slope of the wave packet and the onset of the cooling of the foam is delayed

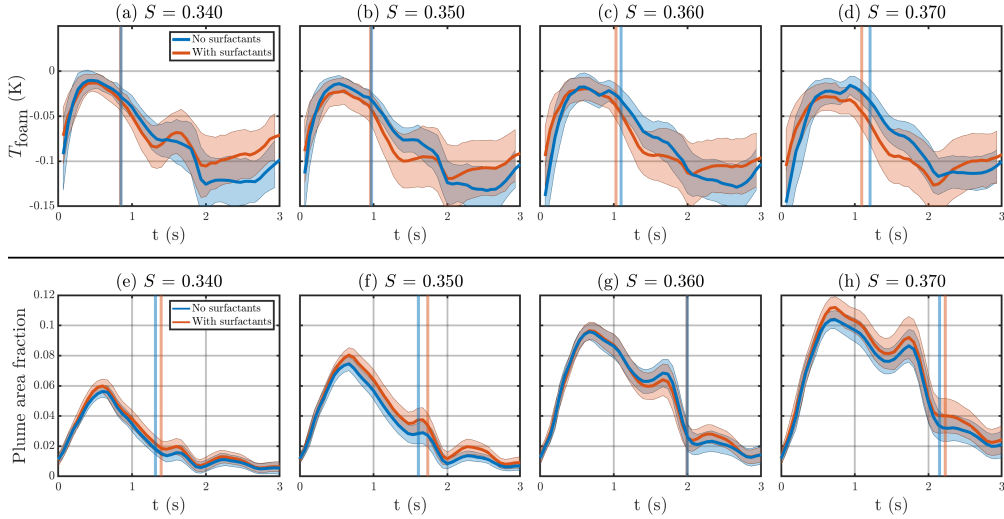


**Figure 9.** The mean foam temperature anomaly versus time (top) and the bubble plume area (bottom), with and without added surfactants. The thick lines are ensemble averages and the shaded areas denote one standard deviations of the samples. The vertical lines indicate the location  $t_{cool}$  for the foam temperature and the e-folding time from the maximum relative to time  $t=0$  for the plume area, which is equal to  $\tau_{plume}^{total}$  (Figure 6).

394 for the larger breakers compared to the smaller ones. Furthermore, the surfactant-free and  
 395 surfactant-added cases follow each other closely in these plots. The time series of the bubble  
 396 plume area from Figure 7(e-h) are repeated in Figure 9(e-h) with the time axis expanded  
 397 to correspond to the temperature anomaly plots.

398 Surface foam and subsurface bubbles are generated immediately after the breaking  
 399 process begins. As shown in Figure 5, the evolution of the thermal signature of foam also  
 400 commences immediately after breaking starts, beginning as an increase in temperature due  
 401 to the disruption of the cool skin. Therefore, we define the time to the onset of cooling,  
 402  $t_{cool}$ , as the time from the start of breaking to when the mean foam temperature anomaly  
 403  $T_{foam}$  falls below its maximum value by a fixed amount. That amount was taken to be the  
 404 minimum detectable temperature change given by the noise level of the infrared camera  
 405 (NEDT of 0.025 K). For comparison of  $t_{cool}$  to the bubble plume timescale, we use the  
 406 total bubble plume timescale,  $\tau_{plume}^{total} = \tau_{plume}^{decay} + t_{plume}^{max}$ , defined as the bubble plume decay  
 407 timescale plus the time from the start of breaking to  $A_{plume}^{max}$ , the time of maximum bubble  
 408 plume area (Figure 6). The use of these timescales based on the time since the beginning  
 409 of breaking is consistent with the recent approach by Callaghan (2018), who used the sum  
 410 of the growth and decay phase timescales as the appropriate timescale for determination of  
 411 whitecap coverage. The onset of cooling and the total bubble plume timescale are indicated  
 412 in the corresponding time series in Figure 9 by vertical lines for both surfactant-free and  
 413 surfactant-added cases.

414 The plot of  $t_{cool}$  versus the total bubble plume timescale  $\tau_{plume}^{total}$  in Figure 10(a) shows  
 415 an approximately linearly relationship. Small differences in the onset of cooling between  
 416 the surfactant-free and surfactant-added cases are apparent for the two largest slopes (see  
 417 also Figure 9(g-h)). However, these differences between the surfactant-free and surfactant-  
 418 added cases are within the experimental variation, indicated by the standard deviation of the  
 419 ensemble, and are thus not considered statistically significant. The lack of significant effect of  
 420 surfactants on  $t_{cool}$  is consistent with previous observations that have examined evaporation  
 421 suppression by surfactant added to water. Some surfactants have the ability to reduce

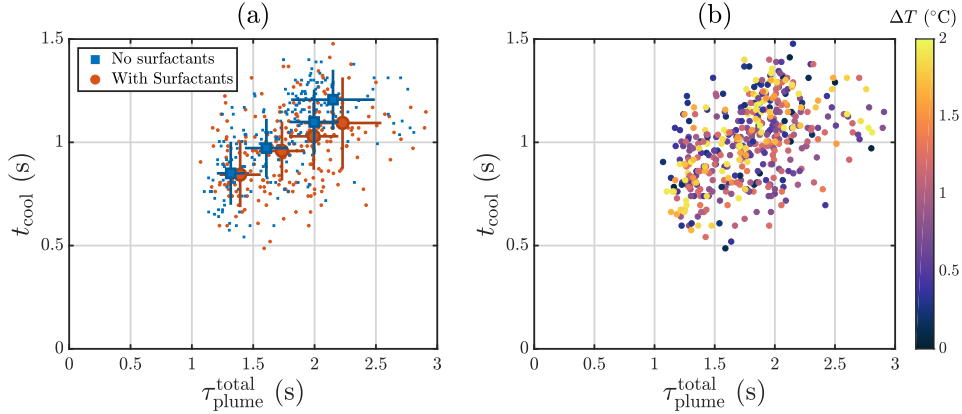


**Figure 10.**  $t_{\text{cool}}$  versus  $\tau_{\text{plume}}$  (a) The small symbols represent individual runs. The large symbols are the ensemble-averaged values at each condition and the error bars show one standard deviations. (b) Each circle represents one experimental run and is colored based on the water-air temperature difference,  $\Delta T$ , shown in the colorbar.

422 evaporation through the formation of a monolayer (Barnes, 1986), reducing outward heat  
 423 flux and suppressing surface cooling. However, this layer is relatively fragile, and mechanical  
 424 agitation by wind and strong surface turbulence, such as the action of wave breaking and  
 425 foam generation, will disrupt it and negate any evaporation resistance (Katsaros & Garrett,  
 426 1982). The strong and roughly linear correlation between  $t_{\text{cool}}$  and  $\tau_{\text{plume}}^{\text{total}}$  implies that the  
 427 time to the onset of cooling can be used as a proxy for the total bubble plume timescale  
 428 without a significant impact of surfactants.

429 We also examined the effect of the ambient heat flux by varying the air-water temper-  
 430 ature difference for each experimental run, shown in Figure 10(b). Each individual data  
 431 point from Figure 10(a) is colored by the temperature difference between the water and the  
 432 air,  $\Delta T = T_{\text{water}} - T_{\text{air}}$ . The lack of a discernible relationship over the two degree range of  
 433  $\Delta T$ , similar to ocean conditions, indicates that the onset of cooling is not strongly affected  
 434 by the air-water heat flux.

435 The generated breaking events initially produce a single foam patch and corresponding  
 436 bubble plume that then quickly separates into two distinct foam patches and bubble plume  
 437 pairs, as shown in the time sequences from an individual run in Figure 4. The distinct foam  
 438 patches and associated bubble plumes are generated at different times and with different  
 439 intensities and thus differ in their spatial and temporal evolution. For instance, the trailing  
 440 bubble plume in Figure 4(c-e, bottom) is nearly dissipated in Figure 4(f, bottom) when  
 441 the leading plume is still robust, which is not necessarily reflected in the evolution of the  
 442 foam patches in the corresponding panels in Figure 4. The occurrence of two separately  
 443 evolving bubble plumes and corresponding foam patches suggests that separately tracking  
 444 and measuring the evolution of  $t_{\text{cool}}$  and  $\tau_{\text{plume}}^{\text{total}}$  for one foam-plume pair may improve the  
 445 correlation.

446 The analysis region for individual foam patches was identified and tracked using ensemble-  
 447 averaged intensity images for each slope and surfactant condition, as illustrated by the se-  
 448 quence in Figure 11 (top) for  $S = 0.37$  without additional surfactants. Each image is the  
 449 result of averaging the same frame of foam masks relative to the start of breaking, among all  
 450 the runs with the same conditions. Therefore, the intensity value at each pixel is equal to the  
 451 fraction of runs in which the pixel was covered by foam or bubbles. The ensemble averaging  
 452 of the foam images reveals the well defined two-dimensional structure of the foam. The  
 453 single transverse strip of foam in Figure 11(a) quickly separates into two transverse strips in

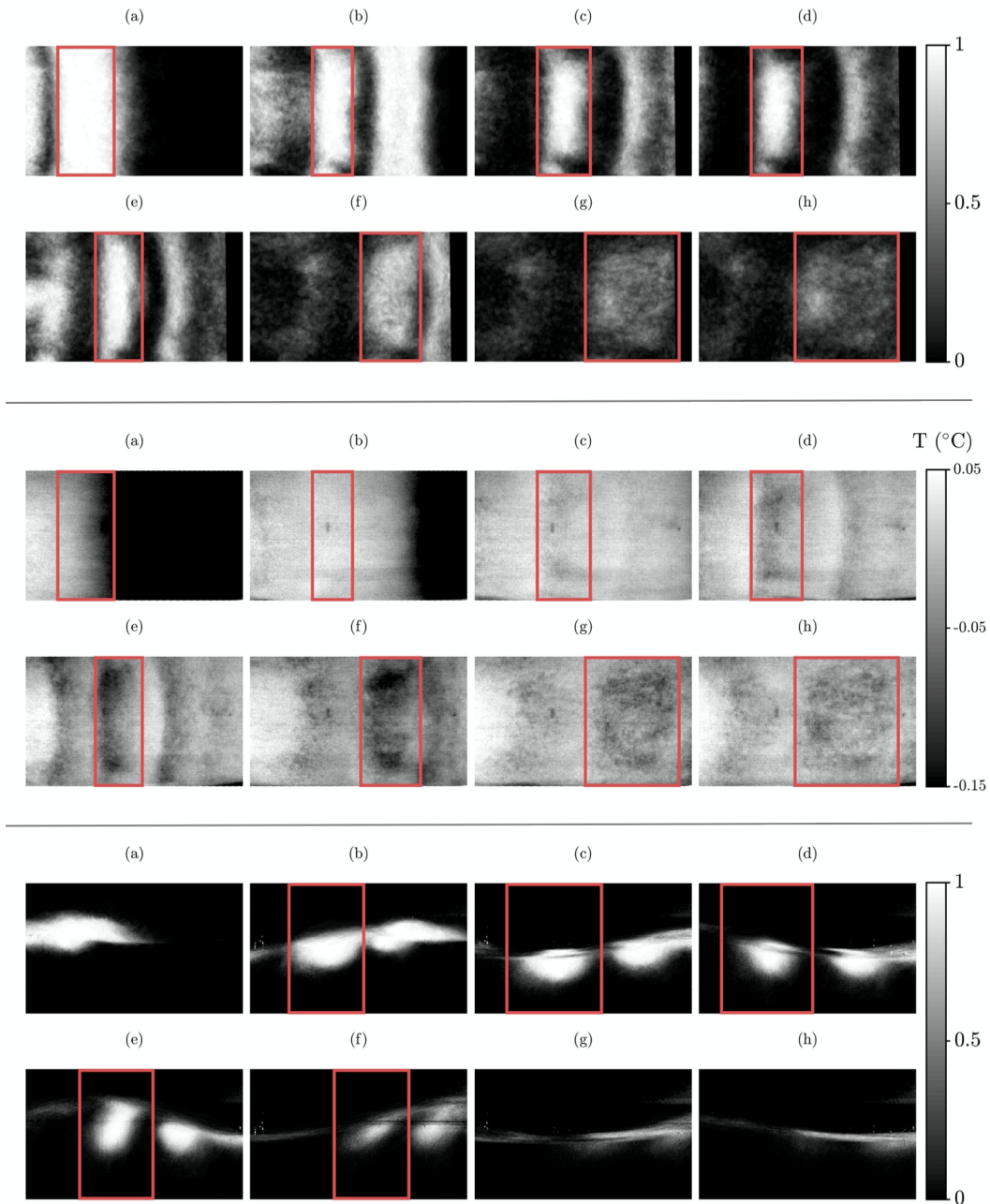


**Figure 11.** A sequence of ensemble-averaged intensity images of the foam (top), the surface temperature (middle), and the bubble plume (bottom) for the experimental condition with a slope of 0.37 without additional surfactants. The red box follows the most salient foam patch (and the corresponding bubble plume) of the breaker and shows the region that is used in analyzing the foam temperature and the plume area. This figure corresponds to Movie S4 in the supplementary information.

454 Figure 11(b) that continue to propagate down the tank as separate features. The rectangular  
 455 box overlaid on each image corresponds to the portion of the image used in analyzing the  
 456 foam temperature in the individual run sequences of infrared imagery. The location and the

width of the tracking box were defined manually by inspecting the ensemble-averaged foam images with the goal of containing most of the foam in a strip. Note that the tracking boxes were calculated based on the ensemble-averaged foam data and then applied to infrared images from individual runs with the same conditions. The corresponding bubble plume is similarly tracked using the ensemble-averaged bubble plume images (Figure 11, bottom) and then applied to individual runs. The location and width of the tracking window for the bubble plume were defined independently of the tracking window for the foam data. The reason was that the bubble plume is deformed greatly by the fluid motion at depth due to the waves and is not necessarily located directly beneath the foam strip.

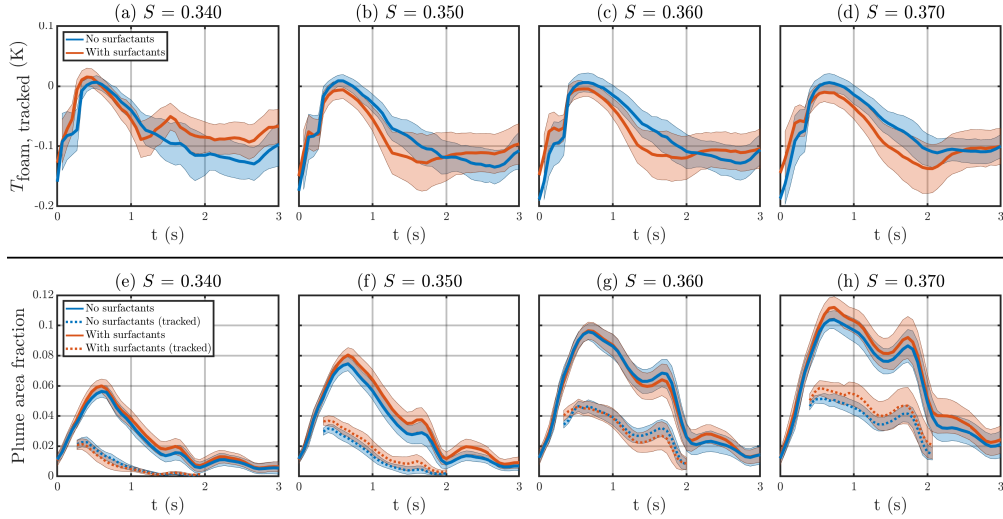
The mean temperature of the foam in the tracking box is plotted versus time in Figure 12(a-d). Similar to the results of Figure 9 for the whole field of view, the onset of cooling of the foam is delayed with the scale of the breaking strength, given by the wave packet slope,  $S$ . The difference between the surfactant-free and surfactant-added cases is once again relatively small. The bubble plume was similarly tracked as shown in Figure 11 (bottom). However, obtaining the time scale for individual bubble plumes proved to be problematic for the cases with the two larger slopes. The reason for this issue can be seen in the plume area time series shown in Figure 12(e-h). The individual bubble plume could only be tracked up to  $t = 2$  s since the separate plumes merged together at that point. Fitting an exponential function to the plume area time series resulted in noisy data due to the lack of data at later stages of decay and the presence of a local peak in the time series caused by the stretching of the bubble plume. However, as can be seen in these plots, the time series for an individual plume follows a trend similar to that for the whole image. Therefore, the maximum depth of the plume,  $d_{\max}$  is used instead of  $\tau_{\text{plume}}^{\text{total}}$  to present the result of tracking an individual plume. The average values of the maximum bubble plume depth for each slope are listed in Table 1.

Figure 13(a) and 13(b) show the time to the onset of cooling,  $t_{\text{cool}}$ , versus maximum depth of the plume for the whole field of view (i. e., both plumes) and for tracking the trailing plume, respectively. For both cases,  $t_{\text{cool}}$  scales with  $d_{\max}$  and the difference between the two surfactant conditions is small (approximately 5% on average). Moreover, the scatter of  $t_{\text{cool}}$  data is less when an individual foam patch was tracked compared to the whole field of view (approximately 0.12 s compared to 0.16 s, respectively). The reduced scatter when tracking a single plume suggests that the spatial variation in  $T_{\text{foam}}$  is related to the spatial variability of the bubble plume depth.

The correlation of the bubble plume depth with the time to the onset of breaking and the observed spatial variability of the foam temperature anomaly suggest that our technique may provide a means of remotely mapping the spatial variability of the plume depth. Our measurement of the bubble plume timescale and depth provide a global measure of the plume characteristics that include a wide range of bubble sizes. However, the delay of the onset of cooling due to the renewal of the foam by rising bubbles is likely associated with a limited range of larger bubble sizes. The onset of cooling may occur because this subset of bubbles responsible for generating the foam are no longer present. Measurements of the distribution of bubble sizes and their subsurface spatial variability combined with infrared temperature maps would be necessary to confirm this implication of our results.

## 5 Conclusions

We presented an experimental investigation of the thermal signature of the residual foam left behind by breaking waves. The experiments were conducted in a saltwater wave tank and breaking waves were generated using the dispersive focusing wave packet technique. We used four different wave packets that had a similar shape but varied significantly in breaking intensity, plume depth, and energy dissipation. For each packet, more than a hundred experiment runs were performed in salt water with and without added surfactants. The visible and thermal signatures of the surface foam produced by the breaking waves



**Figure 12.** (Top) the mean foam temperature anomaly in the tracking box versus time, with and without additional surfactants. Thick lines are ensemble averages and the shaded areas are one standard deviations of samples. (Bottom) bubble plume area normalized by the image size. Solid lines are for the whole field of view and dotted lines are the data inside the tracking window.

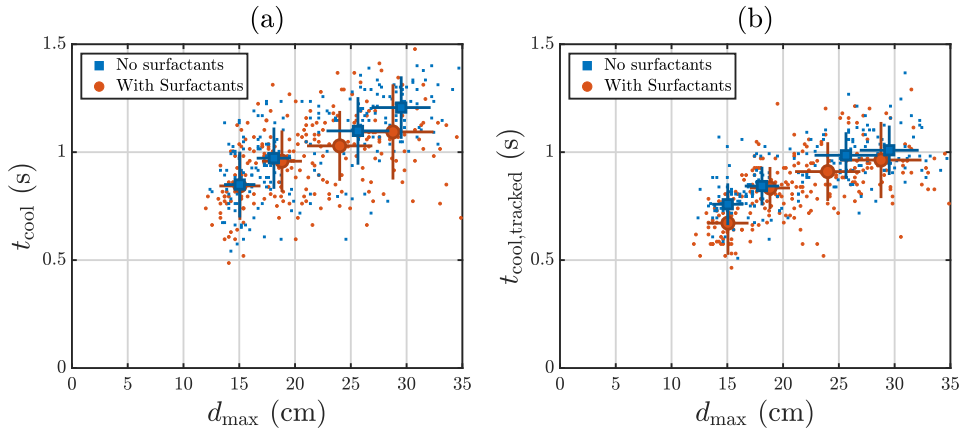


**Figure 13.**  $t_{\text{cool}}$  versus the maximum depth of the plume,  $d_{\text{max}}$  (a) without tracking, and (b) with tracking. The small symbols represent individual runs. The large symbols are the ensemble-averaged values at each condition and the error bars show one standard deviations.

508 were measured. The foam area, bubble plume area, and foam temperature time series  
 509 were calculated from the image sequence data for each experimental run. The visible foam  
 510 timescale,  $\tau_{\text{foam}}^{\text{decay}}$ , the bubble plume time scales  $\tau_{\text{plume}}^{\text{decay}}$  and  $\tau_{\text{plume}}^{\text{total}}$ , and the time to the onset  
 511 of cooling,  $t_{\text{cool}}$ , were evaluated from their corresponding time series.

512 The time to the onset of cooling of the foam,  $t_{\text{cool}}$ , was found to scale with the total  
 513 plume decay time,  $\tau_{\text{plume}}^{\text{total}}$ , and the maximum plume depth. The cooling timescale was  
 514 not significantly affected by the environmental conditions of surfactant concentration and  
 515 air-water temperature difference. Therefore,  $t_{\text{cool}}$  can be used to infer sub-surface plume  
 516 dynamics by quantifying the plume decay time and depth from sea surface temperature  
 517 observations.

518 Our results are consistent with the laboratory result that surface foam cools faster  
 519 than the surrounding clear water due to the enhanced cooling of the bubbles at the surface.  
 520 Furthermore, they support the notion that the cooling of surface foam is delayed until the  
 521 rate of renewal of the foam by rising bubbles is less than the foam cooling rate. Our results  
 522 suggest that the observed spatial variability of  $T_{\text{foam}}$  (Figure 5) may provide information  
 523 about the spatial variability of the bubble plume depth. Adequate investigation of this idea  
 524 will require additional measurements with increased dynamic range of breaking intensity  
 525 and techniques to quantify spatial variability of the bubble plume depth.

## 526 Acknowledgments

527 This work was supported by the National Science Foundation through grant number OCE-  
 528 1736504 and the APL-UW SEED postdoctoral program. We acknowledge Mr. Joseph  
 529 Zacharin for assisting with the experiments, APL Ocean Engineering for engineering and  
 530 modification of WASIRF, and Dr. Morteza Derakhti for helpful discussions. The data  
 531 underlying this paper can be found at this address: <http://hdl.handle.net/1773/45571>.

## 532 References

- 533 Anguelova, M. D., & Webster, F. (2006). Whitecap coverage from satellite measurements: A  
 534 first step toward modeling the variability of oceanic whitecaps. *Journal of Geophysical*  
 535 *Research: Oceans*, *111*(C3).
- 536 Barnes, G. (1986). The effects of monolayers on the evaporation of liquids. *Advances in*  
 537 *Colloid and Interface Science*, *25*, 89 - 200.
- 538 Callaghan, A. H. (2013). An improved whitecap timescale for sea spray aerosol production  
 539 flux modeling using the discrete whitecap method. *Journal of Geophysical Research:*  
 540 *Atmospheres*, *118*(17), 9997-10,010.
- 541 Callaghan, A. H. (2018). On the relationship between the energy dissipation rate of surface-  
 542 breaking waves and oceanic whitecap coverage. *Journal of Physical Oceanography*,  
 543 *48*(11), 2609-2626.
- 544 Callaghan, A. H., Deane, G. B., & Stokes, M. D. (2008). Observed physical and environ-  
 545 mental causes of scatter in whitecap coverage values in a fetch-limited coastal zone.  
 546 *Journal of Geophysical Research: Oceans*, *113*(C5).
- 547 Callaghan, A. H., Deane, G. B., & Stokes, M. D. (2013). Two regimes of laboratory whitecap  
 548 foam decay: Bubble-plume controlled and surfactant stabilized. *Journal of Physical*  
 549 *Oceanography*, *43*(6), 1114-1126.
- 550 Callaghan, A. H., Deane, G. B., & Stokes, M. D. (2017). On the imprint of surfactant-driven  
 551 stabilization of laboratory breaking wave foam with comparison to oceanic whitecaps.  
 552 *Journal of Geophysical Research: Oceans*, *122*(8), 6110-6128.
- 553 Callaghan, A. H., Deane, G. B., Stokes, M. D., & Ward, B. (2012). Observed variation in  
 554 the decay time of oceanic whitecap foam. *Journal of Geophysical Research: Oceans*,  
 555 *117*(C9).
- 556 Callaghan, A. H., & White, M. (2009). Automated processing of sea surface images for the  
 557 determination of whitecap coverage. *Journal of Atmospheric and Oceanic Technology*,  
 558 *26*(2), 383-394.
- 559 Carini, R. J., Chickadel, C. C., Jessup, A. T., & Thomson, J. (2015). Estimating wave energy  
 560 dissipation in the surf zone using thermal infrared imagery. *Journal of Geophysical*  
 561 *Research: Oceans*, *120*(6), 3937-3957.
- 562 Chickadel, C. C., Branch, R., & Jessup, A. T. (2014). Thermal infrared signatures and heat  
 563 flux of sea foam. *American Geophysical Union, Ocean Sciences Meeting*.
- 564 Deane, G., & Stokes, M. (2002). Scale dependence of bubble creation mechanisms in  
 565 breaking waves. *Nature*, *418*, 839-44.
- 566 Drazen, D. A., Melville, W. K., & Lenain, L. (2008). Inertial scaling of dissipation in  
 567 unsteady breaking waves. *Journal of Fluid Mechanics*, *611*, 307-332.
- 568 Duncan, J. H., Qiao, H., Philomin, V., & Wenz, A. (1999). Gentle spilling breakers: crest

- 569 profile evolution. *Journal of Fluid Mechanics*, 379, 191-222.
- 570 Erinin, M. A., Wang, S. D., Liu, R., Towle, D., Liu, X., & Duncan, J. H. (2019). Spray  
571 generation by a plunging breaker. *Geophysical Research Letters*, 46(14), 8244-8251.
- 572 Evans, J., Stride, E., Edirisinghe, M., Andrews, D., & Simons, R. (2010). Can oceanic  
573 foams limit global warming? *Climate Research*, 42, 155-160.
- 574 Fogelberg, R. (2003). *A study of microbreaking modulation by ocean swell using infrared  
575 and microwave techniques* (Unpublished master's thesis). University of Washington.
- 576 Gordon, H. R., & Jacobs, M. M. (1977). Albedo of the ocean-atmosphere system: influence  
577 of sea foam. *Applied Optics*, 16(8), 2257-2260.
- 578 Goshtasby, A. (1986). Piecewise linear mapping functions for image registration. *Pattern  
579 Recognition*, 19(6), 459 - 466.
- 580 Jessup, A. T., Zappa, C. J., Loewen, M. R., & Hesany, V. (1997). Infrared remote sensing  
581 of breaking waves. *Nature*, 385(6611), 52-55.
- 582 Katsaros, K. B., & Garrett, W. D. (1982). Effects of organic surface films on evaporation  
583 and thermal structure of water in free and forced convection. *International Journal  
584 of Heat and Mass Transfer*, 25(11), 1661 - 1670.
- 585 Kiger, K. T., & Duncan, J. H. (2012). Air-entrainment mechanisms in plunging jets and  
586 breaking waves. *Annual Review of Fluid Mechanics*, 44(1), 563-596.
- 587 Kleiss, J., & Melville, W. (2010). Observations of wave breaking kinematics in fetch-limited  
588 seas. *Journal of Physical Oceanography*, 40, 2575-2604.
- 589 Lamarre, E., & Melville, W. (1991). Air entrainment and dissipation in breaking waves.  
590 *Nature*, 351, 469-472.
- 591 Loewen, M. R. (1991). *Laboratory measurements of the sound generated by breaking waves*  
592 (Unpublished doctoral dissertation). MIT/WHOI Joint Program.
- 593 Marmorino, G. O., & Smith, G. B. (2005). Bright and dark ocean whitecaps observed in  
594 the infrared. *Geophysical Research Letters*, 32(11).
- 595 Monahan, E. C. (1969). Fresh water whitecaps. *Journal of the Atmospheric Sciences*, 26(5),  
596 1026-1029.
- 597 Monahan, E. C., & Lu, M. (1990). Acoustically relevant bubble assemblages and their  
598 dependence on meteorological parameters. *IEEE Journal of Oceanic Engineering*,  
599 15(4), 340-349.
- 600 Monahan, E. C., Spiel, D. E., & Davidson, K. L. (1986). A model of marine aerosol  
601 generation via whitecaps and wave disruption. In E. C. Monahan & G. M. Niocaill  
602 (Eds.), *Oceanic whitecaps: And their role in air-sea exchange processes* (pp. 167-174).  
603 Dordrecht: Springer Netherlands.
- 604 Potter, H., Smith, G. B., Snow, C. M., Dowgiallo, D. J., Bobak, J. P., & Anguelova,  
605 M. D. (2015). Whitecap lifetime stages from infrared imagery with implications for  
606 microwave radiometric measurements of whitecap fraction. *Journal of Geophysical  
607 Research: Oceans*, 120(11), 7521-7537.
- 608 Rapp, R. J., & Melville, W. K. (1990). Laboratory measurements of deep-water breaking  
609 waves. *Philosophical Transactions of the Royal Society of London. Series A, Mathe-  
610 matical and Physical Sciences*, 331(1622), 735-800.
- 611 Scanlon, B., & Ward, B. (2013). Oceanic wave breaking coverage separation techniques for  
612 active and maturing whitecaps. *Methods in Oceanography*, 8, 1 - 12.
- 613 Veron, F. (2015). Ocean spray. *Annual Review of Fluid Mechanics*, 47(1), 507-538.
- 614 Wang, A., Ikeda-Gilbert, C. M., Duncan, J. H., Lathrop, D. P., Cooker, M. J., & Fullerton,  
615 A. M. (2018). The impact of a deep-water plunging breaker on a wall with its bottom  
616 edge close to the mean water surface. *Journal of Fluid Mechanics*, 843, 680-721.